Combined In Situ XRD and Ex Situ TEM Studies of Thin Ba$_{0.5}$Sr$_{0.5}$TiO$_3$ Films Grown by PLD on MgO

Sondes Bauer,* Adriana Rodrigues, Xiaowei Jin, Reinhard Schneider, Erich Müller, Dagmar Gerthsen, and Tilo Baumbach

Dedicated to Professor Wolfgang Neumann on the occasion of his 75th birthday

Dielectric barium strontium titanate films were deposited on MgO (001) substrate by pulsed-laser deposition (PLD) and monitored in situ by means of reflection high-energy electron diffraction and time-resolved X-ray diffraction (TRXRD). TRXRD showed two growth periods of the BSTO film and a transformation in the crystalline structure was detected as the thickness exceeds 80 nm. The occurrence of two different crystalline regions, namely BSTO1 and BSTO2 was proved by X-ray diffraction (XRD). Ex situ transmission electron microscopy (TEM) techniques, including diffraction-contrast as well as high-resolution TEM, nanobeam electron diffraction, and scanning TEM in combination with energy-dispersive X-ray spectroscopy reveal structural and microchemical peculiarities of the BSTO film. By these TEM analyses, the presence of the two different regions BSTO1 and BSTO2 within the PLD-grown BSTO layer was demonstrated. Regions of phase BSTO2 were found on top of nanoscaled MgO islands formed on the substrate surface during annealing at high temperature. While the majority phase BSTO1 has a single-crystalline structure over wide ranges, BSTO2 regions seem to be poly- or even nanocrystalline, and the chemical composition of the two phases is also different. The transition in the growth periods is presumably related to the occurrence of BSTO2 regions during layer growth.

1. Introduction

For Ba$_{0.5}$Sr$_{0.5}$TiO$_3$ (BSTO) films grown on MgO, the choice of the growth conditions such as oxygen pressure, substrate selection, and substrate temperature for a certain film thickness has been found to affect the internal strain and the type of tetragonal distortion. In general, assuming the presence of cubic BSTO (space group Pm-3m, lattice parameters $a = b = c = 3.956$ Å) on top of cubic MgO (space group Fm-3m, lattice parameters $a = b = c = 4.214$ Å), the corresponding lattice mismatch would be about 6% and the in-plane lattice of BSTO regions close to the substrate should therefore be tensile strained.

An out-of-plane tetragonal lattice distortion, i.e., a compressively strained BSTO film, was observed in BSTO films grown at a low oxygen deposition pressure (<50 mTorr) by pulsed-laser deposition (PLD), while an in-plane tetragonal lattice distortion, i.e., tensile strain in the BSTO film, was found in films deposited at a high oxygen pressure (>50 mTorr).[1−3] Furthermore, a dependency of the microwave dielectric properties, i.e., dielectric constant, tunability, and dielectric loss, on the oxygen pressure was reported for a BSTO film grown on MgO substrate.[1,4] Zhu et al.[3] recorded the highest dielectric properties for BSTO/MgO grown at 25 Pa (187 mTorr). In the present study, the oxygen pressure was set to 200 mTorr based on the record in the dielectric properties achieved by former investigations.[3] The internal strain changed during the growth

Dr. S. Bauer, Dr. A. Rodrigues, Prof. T. Baumbach
Institute for Photon Science and Synchrotron Radiation
Karlsruhe Institute of Technology
Hermann-von-Helmholtz-Platz 1, Eggenstein-Leopoldshafen D-76344, Germany
E-mail: sondes.bauer@kit.edu

Dr. X. Jin, Prof. R. Schneider, Dr. E. Müller, Prof. D. Gerthsen
Laboratory for Electron Microscopy
Karlsruhe Institute of Technology
Engesserstraße 7, Karlsruhe D-76131, Germany

Prof. T. Baumbach
Laboratory for Application of Synchrotron Radiation
Karlsruhe Institute of Technology
Kaiserstraße 12, Karlsruhe D-76131, Germany

The ORCID identification number(s) for the author(s) of this article can be found under https://doi.org/10.1002/crat.201900235

as the film thickness increases. Theoretical analyses were devoted to determine the dependency of the dielectric properties on the residual strain formed in the grown BSTO/MgO film.[1,5] Chang et al.[1] demonstrated a rapid increase in the dielectric constant when the in-plane tensile strain reaches up to 0.1% while the dielectric constant decreases by further increasing tensile strain as the paraelectric phase changes to the ferroelectric one with the strain-induced polarization. The variation of the dielectric properties with the film thicknesses of BSTO/MgO was investigated by Bellotti et al.[6] for a set of corresponding samples with film thicknesses between 22 nm and 1.15 µm. In their study, the in-plane tensile strains are found to be more favorable for high tunability. However, below a critical thickness of 150 nm the tunability was found to drop off sharply due to a change in the BSTO unit cell. Ex situ investigations using conventional X-ray diffraction (XRD) methods were carried out on a set of samples grown under similar conditions and having different film thicknesses in order to understand the variation of lattice parameters as well as the internal strain with the thickness of the BSTO/MgO film.[6] Furthermore, the internal stress levels are relaxed to a certain extent by the formation of misfit dislocations at the growth temperature when the film thickness exceeds a critical value of 1.5 nm for BSTO with Ba/Sr = 60/40 grown on MgO as it has been calculated by Ban et al.[5] This has revealed a quite different behavior in the dielectric response of BSTO films grown on MgO depending on the film thickness. The calculation of Ban et al.[5] predicted an abnormal increase of the dielectric constant at a critical thickness of 40 nm. However, a further increase in the film thickness would decrease the dielectric constant.

In situ growth analysis by means of synchrotron X-ray diffraction has been demonstrated by Bauer et al.[7] and the references cited therein to be a powerful tool to monitor the crystal structure formed in the grown film as a function of the film thickness. Recently, this favorable and valuable approach was adopted to get insight into the PLD growth of oxide thin films. This approach is based on using simultaneously complementary diagnostic tools like reflection high-energy electron diffraction (RHEED), optical spectroscopic ellipsometry,[7] or multibeam optical stress sensor (MOSS).[8] To our knowledge, simultaneous use of synchrotron XRD and RHEED studies was not yet performed in the case of the PLD growth, but rather in the study of molecular beam epitaxy (MBE) growth processes.[9]

In the present work, it is demonstrated how simultaneous use of in situ RHEED with in situ XRD allows monitoring the growth mode and getting almost complete information about the evolution of the crystalline structure with the film thickness. Because of the known dependency of the dielectric properties of BSTO on the internal strain and the microstructure, one of the aims of this study was to measure as well the residual strain in the film in situ during the PLD growth. The characterization of the crystalline structure of the grown BSTO film was completed by complementary ex situ analyses such as transmission electron microscopy (TEM) for diffraction-contrast as well as high-resolution TEM (HRTEM) imaging, nanobeam electron diffraction (NBD), and scanning TEM (STEM) combined with energy-dispersive X-ray spectroscopy (EDXS) to understand deeper the origin of the change of the structural features with the film thickness and to analyze the chemical composition of the grown BSTO layer.

2. Experimental Section

2.1. PLD Growth of BSTO and In Situ Growth Analysis

BSTO thin films were grown on MgO (100) substrates by pulsed-laser deposition using a frequency quadrupled (266 nm) Nd:YAG laser operated at a repetition rate of 10 Hz and a stoichiometric BSTO target. Pulse duration of 5 ns and a single pulse energy of 63 mJ pulse^{-1} at the target was used. The laser was focused to a spot with a size of 2×1 mm^2 which leads to a fluence of 3.15 J cm^{-2}. The average laser power was 0.63 W at 10 Hz. The substrate was positioned 4 cm away from the target and heated to the growth temperature of $T = 850$ °C using a laser heater with an integrated pyrometer for temperature sensing by an infrared diode laser with a spot size diameter of approximately 10 mm. The oxygen pressure in the chamber was set to 200 mTorr. The alignment of the substrate and the measurement of MgO reflections alone, required for lattice-parameter correction took about 3 h prior to the deposition. As consequence, the MgO substrate had undergone an annealing at $T = 850$ °C for 3 h.

The in situ PLD chamber is equipped with a system for reflection high-energy electron diffraction. The electron gun of this RHEED system was operated at a high voltage of 25 kV and with a current of 1.6 A. The RHEED detector is a fluorescence detector which was positioned in the direction of the reflected beam. The acquisition of RHEED patterns for 1 s was performed during the growth step and saved as movie for further data-analysis procedures. The sample was mounted on a hexapod which has been used to align the sample with respect to the incident X-ray beam and to place it in diffraction geometry. The RHEED gun was inclined to define the incidence angle of 1.7° of the incoming electron beam with respect to the surface. It was possible to monitor the growth by simultaneous recording of the in situ RHEED pattern and the diffraction intensity of the (002) reflection of BSTO termed XRD002 during the first four steps of the growth (see **Figure 1**). Furthermore, the in situ RHEED patterns were recorded during the growth and the recovery steps after shutting off the PLD laser.

2.2. X-ray Data Acquisition Procedure During the Interval PLD Growth

Figure 1d illustrates the procedure for monitoring the PLD growth intervals which consist of alternations between growth and pause steps. Prior to the growth and at the growth temperature of $T = 850$ °C the MgO substrate was aligned with respect to the X-ray beam. Two-dimensional reciprocal space maps (2D-RSMs) of the (002), (004), and (006) symmetric reflections, termed in the manuscript as XRD002, XRD004, and XRD006, respectively, were recorded for MgO in order to be used as a reference for data corrections. During the first four steps of the growth, coupled in situ RHEED patterns and time-resolved X-ray diffraction profiles of the XRD002 reflection of BSTO were simultaneously recorded as it can be seen in Figure 1a,b. Starting with the fifth growth step, the in situ RHEED pattern was getting blurred due to the increase of the film thickness. Only time-resolved X-ray diffraction profiles were then measured to
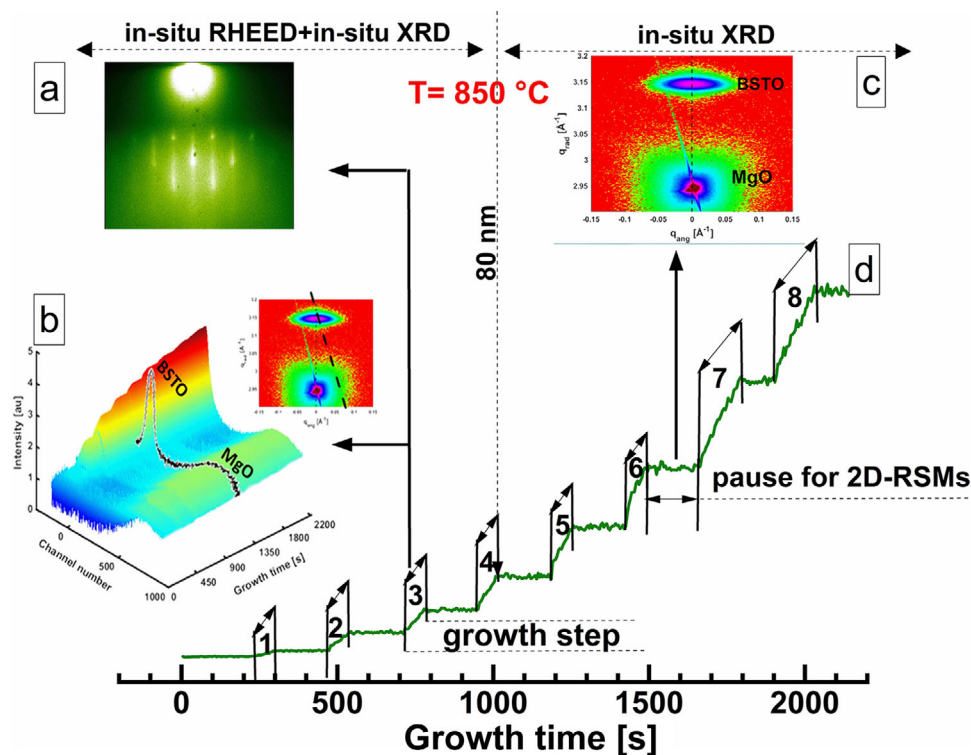
**ADVANCED
SCIENCE NEWS**

www.advancedsciencenews.com

CRYSTAL
Research&Technology

www.crt-journal.org

Figure 1. Schematic presentation of the interval pulsed-laser deposition (PLD) growth procedure. Up to a critical film thickness of $Th = 80$ nm it was possible to combine in situ X-ray diffraction (XRD) with in situ reflection high-energy electron diffraction (RHEED) while above this thickness only XRD measurements were possible. a) Example image of an in situ RHEED pattern recorded during the third growth step. b) 3D time-resolved diffraction intensity of the XRD002 reflection of BSTO at fixed detector position recorded during the complete interval growth process. c) Example image of a two-dimensional reciprocal space maps (2D-RSM) of XRD reflections recorded during the pause steps while the laser is shut off. d) Variation of the recorded intensity I_{002} with the growth time including the growth and pause steps.

control the variation of the diffracted intensity with the growth time. For in situ XRD002 diffraction measurement of the BSTO peak, the Mythen linear detector was kept at a fixed position in the XRD configuration during all the growth steps. The sample was rotated to the Bragg angle of the BSTO diffraction peak as it is indicated in the 2D-RSM of Figure 1b. The measured profile of the diffraction intensity along the channels of the Mythen detector is drawn in Figure 1b which represents the 3D time scan of the diffraction profile corresponding to the BSTO XRD002 reflection recorded during the interval PLD growth. A more detailed description of the experimental setup is given by Bauer et al.[10] The number of laser pulses was set to 600 for steps 1–6 while the number of pulses was increased to 1200 for steps 7 and 8 (cf. Figure 1d).

Three types of X-ray measurements were performed during all the pause steps, which are briefly described as follows: X-ray reflectivity (XRR) was measured during the pause steps after 1, 2, 3, 4, and 5 min of growth. The fitting procedure using the Leptos software package from Bruker AXS was employed for all XRR curves. Only two fits of XRR curves for $t = 2$ and 4 min are presented in **Figure 2**b. The XRD002 symmetric reflections could be measured for all the pause steps corresponding to the different measured thicknesses while high-order reflections like XRD004 and XRD006, respectively, could only be measured with good statistics for a film thickness larger than 140 nm. Two-dimensional reciprocal space maps of the XRD002

reflection were recorded by means of rocking curve scans which were carried out by rotating the whole chamber around the vertical axis in Bragg conditions, while the detector was kept at the respective Bragg diffraction angle in the horizontal diffraction plane. Moreover, 2D-RSMs at grazing incidence were acquired from the grazing incidence (200), (400), and (600) diffraction spots, termed GID200, GID400, and GID600, respectively, for all growth steps by rotating the sample mounted on the hexapod around its normal while keeping the detector at the respective Bragg diffraction angle in the vertical diffraction plane. Due to the weakness of the diffracted intensity of high-order reflections, GID400 and GID600 could only be measured for a film thickness above 140 nm. It should be noted here that high-order reflections were used for an accurate determination of the wave scattering vectors and therefore of the corresponding out-of-plane and in-plane lattice parameters.

2.3. Ex Situ TEM Characterization

Structural and microchemical investigations of the deposited BSTO layer in cross-section perspective were performed by TEM, in particular by diffraction contrast and HRTEM imaging, NBD, and STEM combined with EDXS. For this purpose, an electron-transparent specimen was prepared by focused ion beam (FIB)
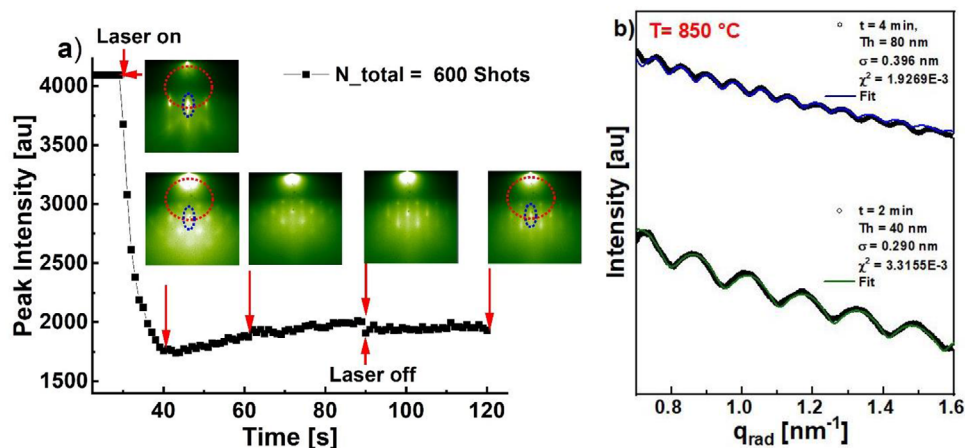
**ADVANCED
SCIENCE NEWS**

www.advancedsciencenews.com

CRYSTAL
Research & Technology

www.crt-journal.org

Figure 2. a) The variation of the reflection high-energy electron diffraction (RHEED) peak intensity as recorded in situ with time during about 120 s, where the first 60 s correspond to the effective growth step between laser on and laser off, exemplary RHEED patterns acquired at a given time are illustrated together with the curves for 600 pulses. b) X-ray reflectivity curves corresponding to the growth time of $t = 2$ and 4 min. The fitting curves were derived by using the Leptos software package.

milling using an FEI Dual Beam Strata 400S instrument. Before FIB preparation of the TEM lamella, the BSTO surface was protected by depositing a Pt/C layer on the top of the sample. Coarse FIB milling was performed at 30 kV accelerating voltage with Ga^+ ions, whereas the lamella surfaces were finally polished via ≈10 000 scans at each side at 5 kV and 70 pA ion current.

TEM studies were carried out by using a 200 kV FEI Tecnai Osiris and a 300 kV FEI Titan 80-300 transmission electron microscope, which both are equipped with thermally assisted field-emission electron guns. Because of the advantageous and special features of the three condenser lenses of the Titan microscope, it is possible to set up an electron probe with a size of approximately 8 nm and a convergence angle of only about 0.6 mrad, thus the beam profile is nearly parallel which allows to perform NBD experiments. STEM images were taken via the high-angle annular dark-field (HAADF) detector, which yields atomic-number contrast. The Osiris microscope has an FEI ChemiSTEM detector with four silicon drift detectors (SDD) for high-efficiency EDXS analyses. With this device, 2D element-specific maps were recorded at high lateral resolution by combined STEM−EDXS. For X-ray mapping, the measuring time amounted to typically 1–2 h, and any possible specimen drift was corrected by the Esprit software (Bruker). This software was also used for quantification of the obtained EDXS data on the basis of the thin-film approximation.[11]

2.4. Data Analysis Procedures

2.4.1. Thickness Determination

The thickness of the grown BSTO film was derived from the fitting of XRR curves for the five growth steps. The fitting was performed using the Leptos package and is shown in Figure 2b. The achievable film thickness after 1 min duration of 600 pulses was estimated to be 20 nm.

2.4.2. In Situ RHEED Intensity Variation

The RHEED patterns were analyzed using the kSA 400 software (k-Space Associates, Inc.). The intensity variation with the growth time was derived from the peak intensity of a sharp diffraction spot (labelled by a dotted blue ellipse in Figure 2a) lying on the zeroth-order of the Laue circle (shown by a dotted red circle in Figure 2a). RHEED patterns were recorded for 120 s where 60 s correspond to the growth time indicated by the two data points (laser on and laser off) in Figure 2a. Furthermore, the variation of the peak intensity during the recovery phase was also recorded.

2.4.3. Time Resolved X-ray Diffraction

Time-resolved X-ray diffraction (TRXRD) data were collected by measuring the intensity profile of the XRD002 reflection of BSTO during all growth steps and during a pause of 2 min after shutting off the PLD laser to control variation of the intensity. The distribution of the intensity over the channels was drawn by the solid-line profile (cf. Figure 1b). This profile corresponds to a cut in the 2D-RSM along the continuous black line crossing the maximum peak intensity of the XRD002 reflection of the BSTO as it is illustrated in Figure 1b. The integrated area of the diffraction profiles determined during the growth steps and the pause time of 2 min was given by step profiles as shown in Figure 1d. The variation of the XRD002 intensity with growth time is presented in a 3D-plot in Figure 1b. Afterwards, the variation of the diffracted intensity I_{002} with the growth time was derived without considering the pause step (see Figure 5b).

2.4.4. In-Plane and Out-of-Plane Lattice Parameters

From each recorded 2D-RSM of the XRD002 and GID200 reflections, a vertical scan at $q_{ang} = 0°.Å^{-1}$ along the vertical dashed line

**ADVANCED
SCIENCE NEWS**

www.advancedsciencenews.com

CRYSTAL
Research&Technology
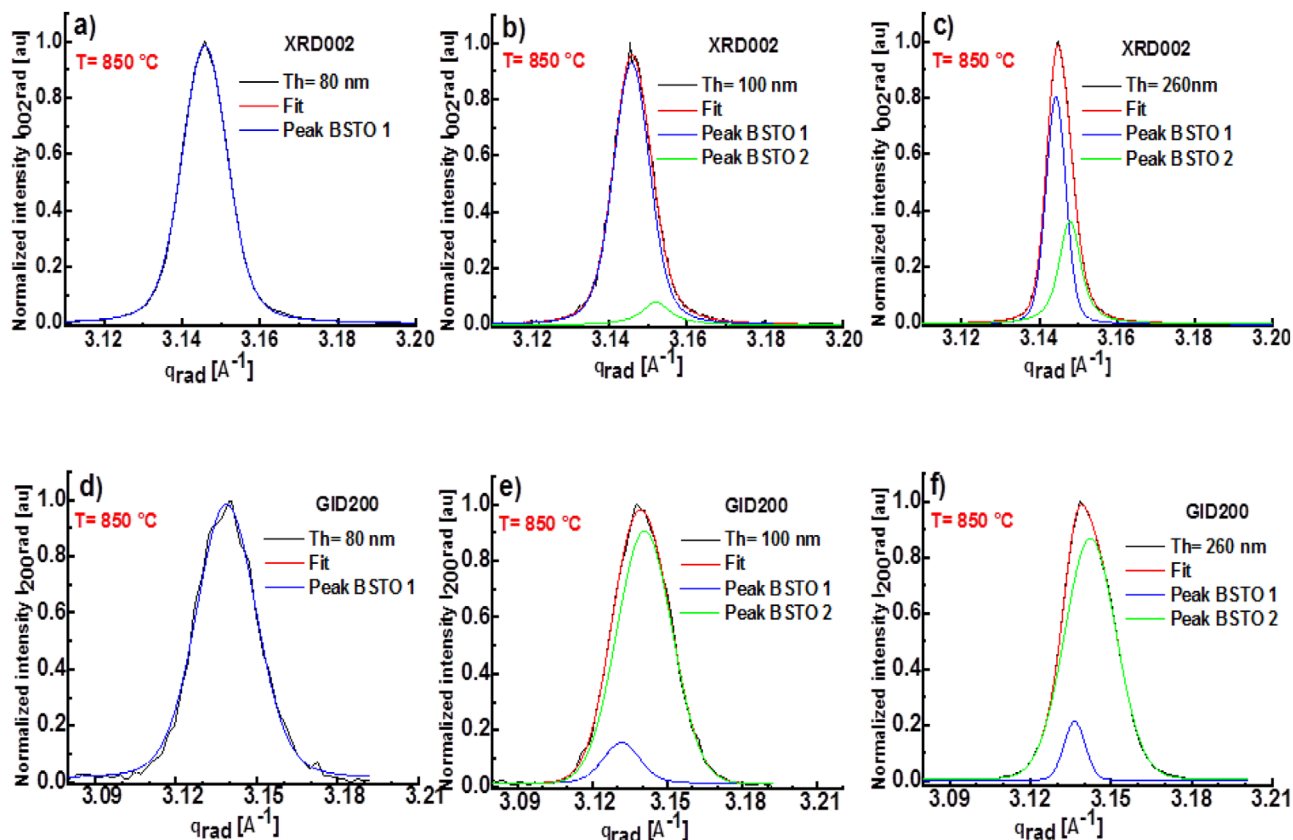
www.crt-journal.org

Figure 3. The curves in a–c) represent the radial intensity profiles I_{002} of the XRD002 symmetric reflection and corresponding fitting profiles using a multiapproach method for thicknesses $Th = 80$, 100, and 260 nm; d–f) show the radial profiles I_{200} of the GID200 reflection together with fitting profiles (multiapproach method) for thicknesses $Th = 80$, 100, and 260 nm.

(see, e.g., 2D-RSM in Figure 1c) and radial diffraction profiles were derived to determine the out-of-plane and the in-plane lattice parameters, respectively. Exemplarily, for thicknesses of 80, 100, and 260 nm of the BSTO layer corresponding profiles are given in **Figure 3**. These radial diffraction profiles of the XRD002 and GID200 reflections were fitted to a linear combination of Voigt profiles using the multistart approach, and the resulting fit curves are also drawn in Figure 3. The fitting procedure was described in detail by Bauer et al.[11]

The out-of-plane lattice parameters $c1 = 2 \times (2\pi/Qc1)$ and $c2 = 2 \times (2\pi/Qc2)$ corresponding to the crystalline BSTO1 and BSTO2 regions were determined from the corresponding peaks positions $Qc1$ and $Qc2$. In similar manner, the in-plane lattice parameters $a1 = 2 \times (2\pi/Qa1)$ and $a2 = 2 \times (2\pi/Qa2)$ were derived from the peak positions $Qa1$ and $Qa2$ of the fitted GID200 reflections profiles. The variation of the unit-cell parameters with the film thickness for the BSTO1 and BSTO2 regions during the PLD-growth is illustrated in **Figure 4**.

2.4.5. Determination of the Proportions of the BSTO1 and BSTO2 Phases

The dominance of the BSTO phases was measured by determining the proportion of BSTO1 and BSTO2 regions X_{BSTO1}[%] and

X_{BSTO2}[%] given as below:

$$X_{BSTO1} = A1/ (A1 + A2) \text{ and } X_{BSTO2} = A2/ (A1 + A2)$$

where $A1$ and $A2$ are the integrated areas of the diffraction profiles of XRD002 reflections.

2.4.6. In-Plane Residual Strain $\varepsilon_{//}$

Similarly to the procedure applied and described in details by Segmüller[12] and Bauer et al.,[11] respectively, the in-plane residual strain was determined from the in-plane and out-of-plane lattice parameters using the following formula:

$$\varepsilon_{//} = \frac{[a1/2 - a01/02]}{a01/02}$$

where

$$a01 = \frac{\left[c1 + 2\left(\frac{c_{12}}{c_{11}}\right)a1\right]}{\left[1 + 2\left(\frac{c_{12}}{c_{11}}\right)\right]} \quad a02 = \frac{\left[c2/2 + 2\left(\frac{c_{12}}{c_{11}}\right)a2\right]}{\left[1 + 2\left(\frac{c_{12}}{c_{11}}\right)\right]}$$

**ADVANCED
SCIENCE NEWS**

www.advancedsciencenews.com

CRYSTAL
Research & Technology
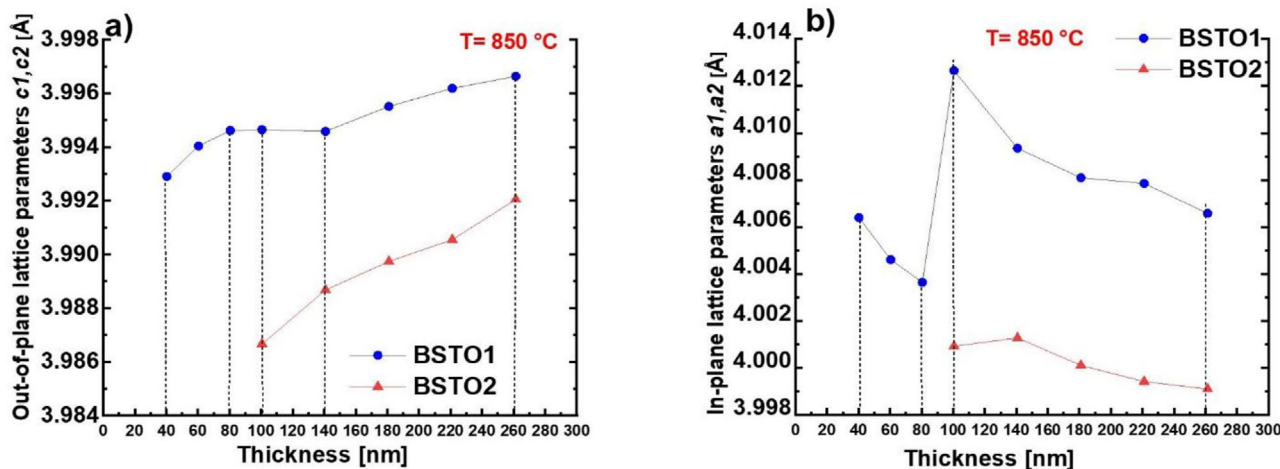
www.crt-journal.org

Figure 4. a) Comparison of the out-of-plane lattice parameters determined from the BSTO1 (blue solid circle) and BSTO2 (red triangle) regions as function of the film thickness. b) Comparison of the in-plane lattice parameters of the BSTO1 (blue solid circle) and BSTO2 (red triangle) regions as function of the film thickness.

where $a1/2$ and $c1/2$ are the in-plane and out-of-plane lattice parameters of the BSTO1 and BSTO2. c_{ij} are the elastic constants of BSTO1 and BSTO2, $c_{11} = 3.11645 \times 10^{11}$ N m^{-2} and $c_{12} = 1.39805 \times 10^{11}$ N m^{-2} which were obtained by weighted averaging of the elastic constants of bulk SrTiO$_3$ and BaTiO$_3$ single crystals.

2.4.7. Tetragonal Distortion D

The tetragonal distortions $D1$ and $D2$ of BSTO1 and BSTO2 were determined and monitored for the different growth steps as $D1 = a1/c1$ and $D2 = a2/c2$.

3. Results and Discussion

We have studied the evolution of the crystalline structure of BSTO films in terms of lattice parameters and residual strain as a function of the film thickness using in situ synchrotron X-ray diffraction during the growth at a temperature of $T = 850$ °C. Moreover, we accomplished these analyses by ex situ TEM diffraction contrast as well as HRTEM imaging, NBD experiments, and combined STEM−EDXS analyses in order to characterize the crystalline and microchemical nature of the different BSTO regions within the layer at room temperature.

3.1. In Situ Monitoring of the PLD Growth of the BSTO Film

During BSTO deposition, in situ RHEED could be combined with in situ XRD of the 002 diffraction peak intensity up to 80 nm thicknesses, where it was possible to record RHEED pattern movies for the four first steps of growth (see Figure 1).

Figure 2a presents the variation of the intensity marked with a dashed blue ellipse as well as selected RHEED patterns at $t = 30$ s for the substrate before the start of the growth, at $t = 40$ s (i.e., 10 s of growth), $t = 60$ s, and $t = 90$ s when the laser was shut off and

at $t = 120$ s during the recovery phase. The thickness of the film for 60 s of growth is estimated from XRR curves to be 20 nm. It should be noted that the in situ RHEED patterns had remarkably changed from a spotty pattern at $t = 40$ s to elongated diffraction streaks with additional spots forming on the 2D streaks indicating the occurrence of a mixed growth, namely of a 2D layer with additional 3D objects. In more detail, these streaks arise from finite-size effects and are characteristic of a 2D surface structure with a limited lateral correlation length. The appearance of spots on the streaks indicates the formation of 3D objects on top of the 2D layer.

Two XRR curves (Figure 2b) correspond to the growth times of 2 and 4 min and give a growth rate of 20 nm min^{-1}, where the roughness increases from 0.290 to 0.396 nm, respectively.

The intensity distribution along the Mython detector channels was recorded during the growth steps of 1 min and during the pause step of 2 min. As a result, a 3D-intensity distribution was derived from the TRXRD study and is presented in Figure 1b. It is worthwhile to point out that the diffracted intensity remains constant when the PLD laser is shut off, indicating an equilibrium state of the growth as it can be shown in Figure 1d. At equilibrium state and during the pause steps, the corresponding 2D-RSMs for each growth step were recorded. As it is illustrated by the 3D-intensity distribution (Figure 2b), only the intensity of the BSTO peak is increasing while the peak intensity of MgO remains the same.

To better understand the growth mechanism and the corresponding crystalline and morphological transformations as a function of the film thickness, diffraction profiles of XRD002 and GID200 were analyzed by employing a multiapproach fitting procedure. Exemplarily, in Figure 3 only graphs corresponding to the thicknesses 80, 100, and 260 nm are shown. Three regions in the variation of the lattice parameters for BSTO can be distinguished.

For a film thickness $Th \leq 80$ nm, one single-crystalline BSTO1 region was found with one in-plane lattice parameter $a1$ and an out-of-plane lattice parameter $c1$. Therefore, the radial diffraction profiles of XRD002 and GID200 are well symmetric and can be fitted accurately with one single Voigt profile as it is illustrated in
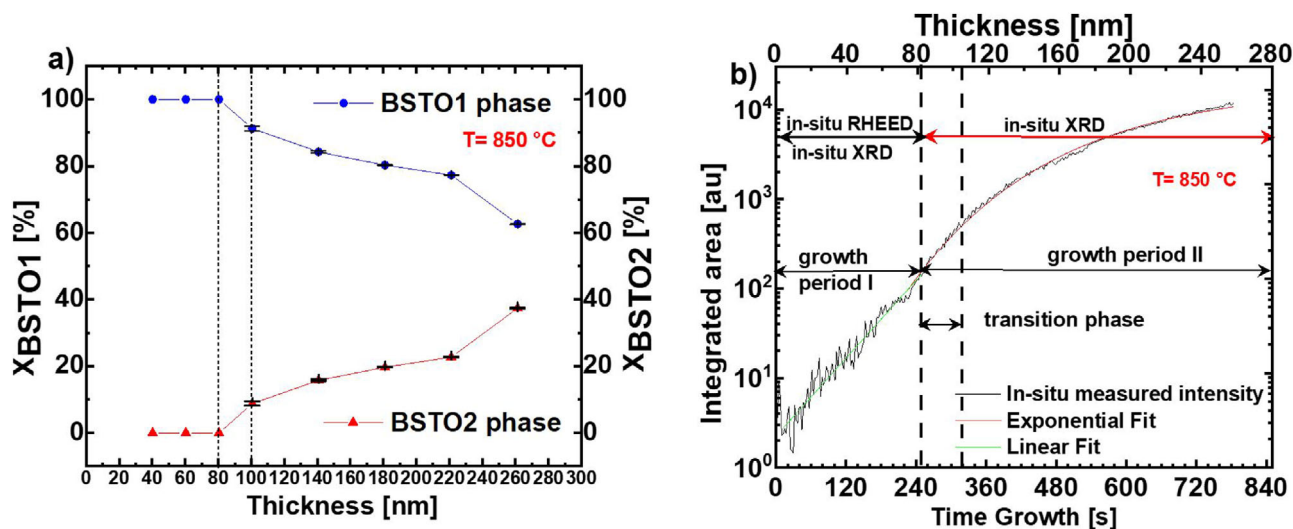
ADVANCED
SCIENCE NEWS
www.advancedsciencenews.com

CRYSTAL
Research&Technology
www.crt-journal.org

Figure 5. a) Variation of the portions of the BSTO1 and BSTO2 regions with the film thickness. b) Variation of the diffracted intensity determined by the integrated area of the radial profile of the XRD002 reflection as a function of growth time and film thickness, respectively, indicating the existence of two growth periods I and II.

Figure 3a,d. In the following, we define the PLD growth for a film thickness up to 80 nm as period I, where solely one single BSTO phase was detected, and the corresponding fit peak is labelled with BSTO1.

For a film thickness of 80 nm ≤ *Th* ≤ 100 nm, there seems to be a transition from growth period I to a second one (period II), since the diffraction profiles of XRD002 and GID200 become asymmetric. In this case, the profiles could only be fitted by two Voigt functions indicating the presence of two crystalline regions, namely BSTO1 and BSTO2, having different lattice parameters (see Figure 3b,c,e,f). In addition, the radial broadening of the diffraction profiles evidently decreases when the growth period changes from I to II. In this context, by increasing the film thickness beyond 80 nm two crystalline regions BSTO1 and BSTO2 were formed with two different out-of-plane lattice parameters $c1 = 2 \times (2\pi/Qc1)$ and $c2 = 2 \times (2\pi/Qc2)$ which are determined from the corresponding peak positions $Qc1$ and $Qc2$. In Figure 4a, the variation of the out-of-plane lattice parameters is given as a function of the film thickness. In a similar way, in-plane lattice parameters $a1 = 2 \times (2\pi/Qa1)$ and $a2 = 2 \times (2\pi/Qa2)$ were derived from the peak positions $Qa1$ and $Qa2$ of the fitted GID200 reflections and drawn as a function of the film thickness in Figure 4b.

Furthermore, the portions X_{BSTO1} and X_{BSTO2} of the particular BSTO region, i.e., BSTO1 or BSTO2, respectively, were determined from the integrated area of the corresponding radial profile. This allowed us to study the evolution of the dominance of either the BSTO1 or BSTO2 region in situ as a function of the film thickness (see **Figure 5**a). Obviously, the portion of BSTO1 decreases while that of BSTO2 increases, which again indicates a transition from growth period I to II. Finally, this led to a grown BSTO film with a thickness of about 260 nm which is composed of two regions BSTO1 and BSTO2 with approximately $X_{BSTO1} = 63\%$ and $X_{BSTO2} = 37\%$. The variation of the overall BSTO diffracted intensity I_{002} with the film thickness is shown in Figure 5b and displays two growth periods. In the growth period I, the integrated area of the I_{002} peak varies nearly linearly

with the thickness up to about 80 nm while in the growth period II, when the film is getting thicker than 100 nm, it increases exponentially with the thickness.

The increase of the out-of-plane lattice parameter $c1$ of BSTO1 with the thickness Th up to 80 nm (see Figure 4a) was simultaneously accompanied by a decrease of the in-plane lattice parameter $a1$ as it is illustrated in Figure 4b. This had most likely induced a decrease of the tetragonal distortion ratio $D1$ and of the in-plane residual strain of the BSTO1 region. The in-plane lattice parameter $a1$ of the BSTO1 unit cell is expanding while the out-of-plane parameter $c1$ remains unchanged, this means $a1$ (100 nm) > $a1$ (80 nm) and $c1$ (100 nm) = $c1$ (80 nm). Consequently, for the thickness range from 80 to 100 nm an increase of the tetragonal distortion $D1$ of the BSTO1 unit cell can be observed. Starting from a thickness of $Th = 100$ nm, two distinguishable BSTO1 and BSTO2 regions characterized by two different unit cells with ($a1$, $c1$) and ($a2$, $c2$) lattice parameters were detected (cf. Figure 4a,b). For a film thickness $Th > 100$ nm, both regions show a simultaneous increase in the out-of-plane lattice parameters and a decrease of the in-plane parameters, meaning an extension in the normal-surface direction and retraction in the in-plane direction. Additionally, the lattice parameters of BSTO1 are larger than those of BSTO2.

From these results one can deduce that during deposition there was a transition from the growth of one single-crystalline BSTO1 region to two crystalline regions BSTO1 and BSTO2, which occurred when the film thickness increased from 80 to 100 nm. This led to a significant increase of the in-plane residual strain in BSTO1 from $\varepsilon1_{//} = 0.12$ to $\varepsilon1_{//} = 0.24$.

It should be pointed out that the in-plane lattice parameter $a1$ remains higher than the $c1$ value (i.e., meaning $a1 > c1$) which makes the tetragonal ratio higher than 1, meaning that there is tensile strain. For a film thickness above $Th \geq 100$ nm in the growth period II, the asymmetry of the diffraction profiles is interrelated with the existence of two distinguishable crystalline regions BSTO1 and BSTO2 that are characterized by differences

**ADVANCED
SCIENCE NEWS**

www.advancedsciencenews.com

CRYSTAL
Research & Technology

www.crt-journal.org

in their lattices parameters, tetragonal distortion, and in-plane residual strain. Figure 4 also shows the variation of the in-plane and of-out-of-plane lattice parameters of the BSTO2 region. There is clearly an increase of its out-of-plane lattice parameter $c2$ with the film thickness $Th > 100$ nm visible, whereas simultaneously its in-plane lattice parameter $a2$ decreases.

The value of the tetragonal distortion D is known to depend strongly on the oxygen pressure P_{O2}. For P_{O2} higher than 50 mTorr, Alldredge et al.[2] found for BSTO ($x = 0.5$) films deposited by PLD that the in-plane lattice parameters are larger than the out-of-plane parameters ($c > a$ and $D = a/c > 1$). In the case of our BSTO film grown at $P_{O2} = 200$ mTorr, the in-plane lattice parameters $a1$ and $a2$ are always found higher than the out-of-planes parameters $c1$ and $c2$ independent of the film thickness (see Figure 4a,b). The deformation of the unit cell with the thickness exhibits a reverse behavior for the in-plane and out-of-plane lattice parameters for the BSTO1 and BSTO2 regions. Similar phenomena were revealed by Bellotti et al.[6] during an ex situ investigation of the variation of lattice parameters with film thickness for BSTO (60/40) where a set of seven films were grown with thicknesses varying from 22 to 1150 nm at P_{O2} of 100 mTorr and a temperature of 700–800 °C.

As can be deduced from Figure 4, for film thicknesses $Th \leq 80$ nm and $Th \geq 100$ nm the in-plane residual strain decreases with increasing film thickness, which is probably attributed to the occurrence of misfit dislocations during layer growth. Both for BSTO1 and for BSTO2, the in-plane residual strain is reduced to nearly the half of its initial value (more details will be published elsewhere[13]) when the thickness increases from 100 nm up to 260 nm. This should influence the polarization component of the region formed in the grown BSTO film and therefore defines its dielectric response which depends on the in-plane residual strain as well as on the film thickness as demonstrated for BSTO grown on MgO by previous investigations.[5,6,14] Recently, for the BSTO/MgO system the effect of the growth mechanism on the unit-cell strain was theoretically studied by Mukhortov et al.[15] using the algorithm of (generalized technological cycle parameter) structure lattice dynamics properties for the Frank-van der Merwe growth (layer-by-layer) and the Volmer-Weber island growth mechanisms. Following the results of the simulation of Mukhortov et al.[16] in the case of the Volmer-Weber island growth mechanism, an increase of the out-of-plane lattice parameter is expected to be related with a decrease of the in-plane lattice parameter as the film thickness increases, indicating a change from two-dimensional tensile stresses in the substrate plane into compressive stresses. Oppositely, in the case of Frank-van der Merwe growth mechanism, the simulation predicts a simultaneous decrease of the out-of-plane and an increase of the in-plane lattice parameters.

The variation of the lattice parameters of the two BSTO1 and BSTO2 regions with the film thickness drawn in Figure 4 seems to be comparable to the one calculated in the case of the Volmer-Weber mechanism where a 3D-structure is formed on the layer. However, our in situ RHEED features correspond to a mixed layer/island growth, i.e., a so-called Stranski–Krastanov growth, and not to a pure 3D growth. In situ 2D-RSMs recorded during the PLD growth of BSTO at $P_{O2} = 200$ mTorr and at $T = 850$ °C revealed the formation of two crystalline BSTO regions having two different out-of-plane and in-plane lattice parameters when the

thickness exceeds a value $Th = 100$ nm. The in situ study of the PLD growth informs us that the grown BSTO film leads to a film containing BSTO1 and BSTO2 regions with the dominance of BSTO1 with a portion of $X_{BSTO1} = 63\%$. Furthermore, BSTO1 and BSTO2 differ by their in-plane residual strain as well as by their tetragonal distortion. To get more information about the structural peculiarities and the microchemistry of the different BSTO regions, complementary ex situ combined STEM−EDXS investigations were performed, the results of which are demonstrated below.

3.2. Ex Situ Phase Identification of the BSTO Film by TEM Imaging, Electron Diffraction, and Combined STEM−EDXS Analysis

TEM characterization was carried out ex situ on the grown BSTO film cooled down from the growth temperature $T = 850$ °C to room temperature. The bright-field TEM micrograph (**Figure 6**a) shows an overview cross-section image of the BSTO film on the MgO substrate. Evidently, the thickness of the BSTO film varies locally between 275 and 290 nm. Thus, the thickness is found slightly larger than that derived from the total number of pulses and from the growth rate determined from XRR corresponding to the first 4 min of the growth. This difference could be explained by the change of the growth rate that can be inferred from the variation of I_{002} with the film thickness shown in Figure 5b, where the crystalline volume (proportional to the integral intensity of I_{002}) does not increase linearly with growth time. In general, the dark/bright diffraction-contrast features visible within the film hint at the presence of a huge number of dislocations. In more detail, similarly to in situ XRD analysis areas with two different regions can be observed, where BSTO1 represents the most dominant region in the BSTO film being the extensive area surrounding the second region BSTO2 that appears as triangularly shaped contrast features (cf. Figure 6a).

Figure 6b1 depicts a higher magnified image of a transition region between BSTO1 and BSTO2, which is marked by a square in Figure 6a and subsequently called region of interest (ROI) 1. Obviously, owing to distinct differences in the crystallite orientation and/or the crystalline structure, the region of BSTO2 appears here much brighter than the surrounding area of the BSTO1 region. It can evidently be seen that the BSTO2 region has formed across the film thickness in growth direction, while it is limited in the lateral direction. Its lateral size increases from few nanometers at the bottom of the BSTO layer up to about 250 nm for the maximum film thickness of about 280 nm, which clearly hints at the formation of a region with a triangular cross-section during layer deposition. This result is found to be correlated with the increase of the portion X_{BSTO2} of BSTO2 with the film thickness recorded by in situ XRD (see Figure 5a). To demonstrate the structural differences between the BSTO1 and BSTO2 regions, corresponding dark-field images were additionally taken from the BSTO layer. For ROI 1, two typical TEM dark-field images are shown in Figures 6b2,b3, where the first micrograph was obtained with a diffracted beam being typical for the dominant BSTO1 and the latter with one of BSTO2. Already the contrast features observable in the TEM dark-field image of Figure 6b2 hint at some structural disturbance of the
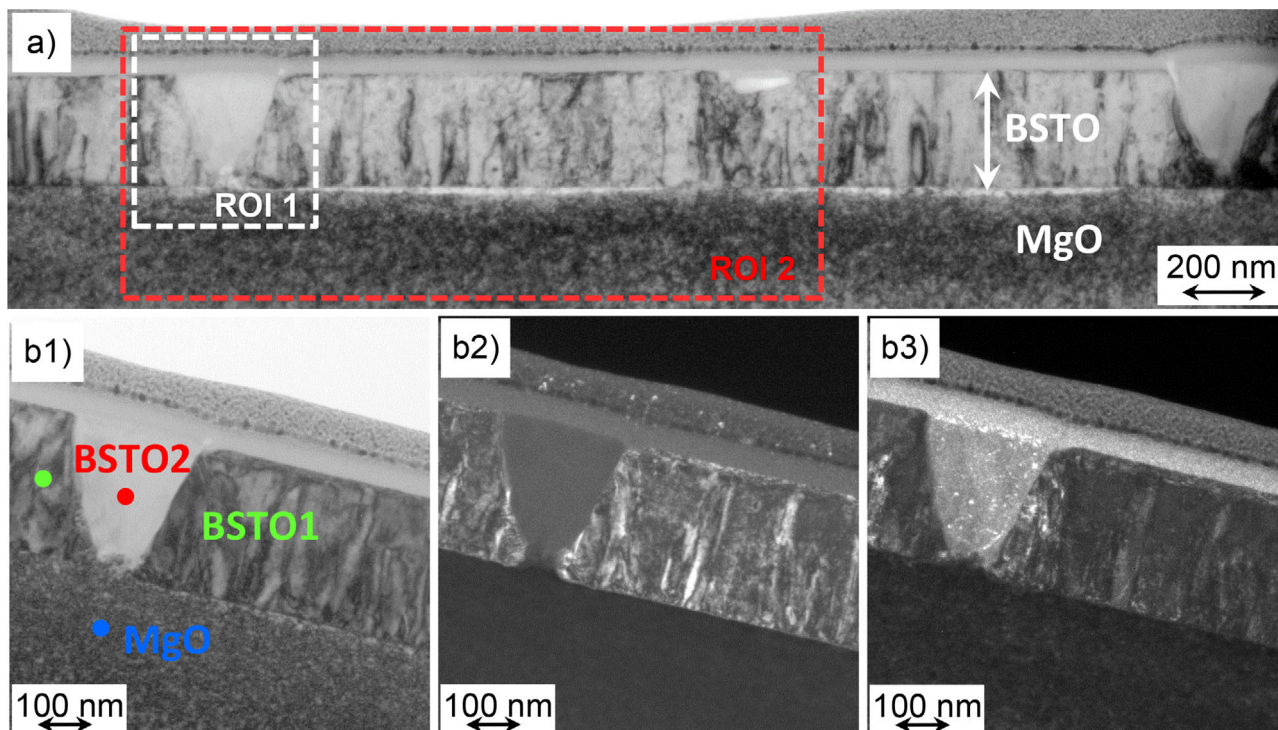
ADVANCED
SCIENCE NEWS
www.advancedsciencenews.com

CRYSTAL
Research&Technology
www.crt-journal.org

Figure 6. Microstructure characterization of the BSTO layer on MgO by diffraction-contrast transmission electron microscopy (TEM) imaging. a) Overview cross-section TEM image of the BSTO layer on MgO; a BSTO region exhibiting a triangularly shaped BSTO2 region is marked by a square (ROI 1) with dashed white lines, while the rectangle of ROI 2 indicates the area whose element distribution is shown in Figure 8. b1) Detailed TEM bright-field image of a transition region (ROI 1) between the dominant BSTO1 and the minor BSTO2 phases, and b2−b3) corresponding TEM dark-field images. The BSTO layer is covered by a Pt layer which was deposited to protect the layer during focused ion beam (FIB) lamella preparation.

transition region between MgO substrate and BSTO2 region. As in the following more clearly shown by HRTEM imaging (see Figure 8c) and, in particular, element mapping via STEM−EDXS (Figure 9e), on the substrate a nanosized MgO island is present.

In order to explore the origin of the structural differences between the BSTO1 and BSTO2 regions, detailed electron-diffraction experiments were performed. However, selected-area electron diffraction is hampered by the small size of the triangularly shaped regions of BSTO2. Even with the smallest selected-area aperture in the Titan microscope, having a diameter of 10 μm, regions of BSTO2 could not be exclusively selected for structural analysis by electron diffraction without contributions of the surrounding material. For this reason, NBD with an 8 nm sized electron probe was applied to analyze the crystal structure of the different regions at positions indicated by the spots colored with blue for MgO, green for BSTO1, and red for BSTO2 in Figure 6b1.

Typical NBD patterns are depicted in **Figures 7**a1 for MgO, 7a2 for BSTO1, and 7a3 for BSTO2 which are compared with diffraction patterns simulated by the JEMS software (see Figures 7b1–b3).[12] In more detail, in Figure 7a1 the NBD pattern taken from the MgO substrate close to ROI 1 is shown. The simulated diffraction pattern in Figure 7b1 agrees well with the experimental pattern assuming cubic MgO (space group Fm-3m, lattice parameters $a = b = c = 4.214$ Å, ICSD code 52 026) oriented along a [010] zone axis. A typical NBD pattern of BSTO1 (taken at the green spot in Figure 6b1 to the left of the BSTO2 region) is presented in Figure 7a2. The pattern taken at the right

side of the BSTO2 region (not shown here) looks very similar. In the case of BSTO1, the simulation of diffraction patterns using crystal-structure data of cubic BSTO (space group Pm-3m, lattice parameters $a = b = c = 3.956$ Å, COD code 1 512 123) yields a good agreement with the pattern expected for BSTO along its [010] zone axis. In general, apart from slight local orientation variations, all experimentally recorded diffraction patterns of the BSTO layer in the BSTO1-rich regions are similar and typical for single-crystalline BSTO along a ⟨100⟩ zone axis.

The triangle-shaped region BSTO2 in Figure 6b1 exhibits a different diffraction pattern as visible in Figure 7a3. It seems to be the result of a superposition of at least three diffraction patterns, one pattern with intense reflections and two or even more patterns with weak reflections. The comparison of the experimental pattern of BSTO2 with simulations shows that the main reflections can be described by a diffraction pattern simulated for BSTO with cubic structure and oriented along its [313] zone axis (see Figure 7b3). Further detailed analyses of the additional weak reflections reveal that most of them are probably caused by BSTO nanocrystals with cubic (space group Pm-3m) structure, but with different zone-axis orientations. However, a few of the additional reflections might agree with diffraction intensities calculated for hexagonal BSTO (space group P6₃mc, $a = b = 5.7238$ Å, $c = 13.9649$ Å, ICSD code 75 240). Therefore, from these findings we conclude that the triangularly shaped BSTO2 regions are nanocrystalline and composed of larger crystallites with the cubic structure of BSTO and a few smaller ones, which presumably have a different crystal structure. This structural
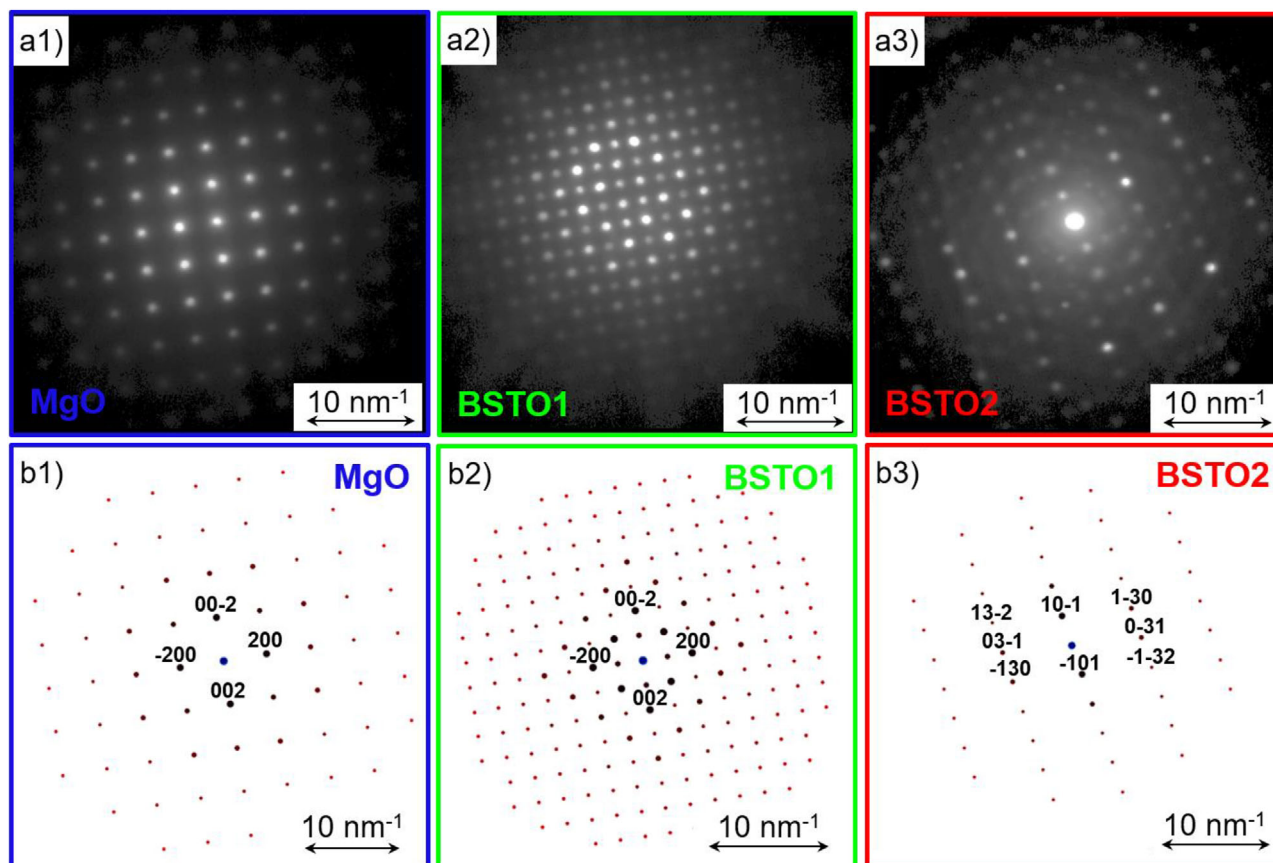
**ADVANCED
SCIENCE NEWS**

www.advancedsciencenews.com

CRYSTAL
Research&Technology

www.crt-journal.org

Figure 7. Structure analysis of the BSTO layer on MgO by nanobeam electron diffraction, a1–a3) represents the nanobeam electron diffraction (NBD) patterns of the areas marked in Figure 6b1 by a blue spot for the MgO substrate, green spot for the BSTO1-containing region, and red spot for the BSTO2 region, respectively. In b1–b3) simulated diffraction patterns are depicted for MgO as well as the BSTO1 and BSTO2 regions.

setup is found for all such BSTO2 regions and, thus, appears to be typical for the PLD-grown BSTO layer under investigation.

To get a deeper insight into the structural peculiarities of the PLD-grown BSTO film, particularly regarding differences between the BSTO1 and BSTO2 regions, HRTEM imaging was additionally performed. Typical results for the different interface regions, i.e., between the MgO substrate and BSTO1 or BSTO2, respectively, as well as between BSTO1 and BSTO2, are given in **Figure 8**. In general, all regions of BSTO1 show a good crystallinity and also a well-defined orientation relationship with respect to the underlying MgO substrate. Exemplarily, this can be concluded from Figure 8a which depicts a BSTO1/MgO transition region where the corresponding interface is marked by an arrow. Here, the direction of the electron beam is parallel to the [100] zone axis of MgO. The insets in the lower and upper right corners show diffractograms that were obtained by Fourier transformation of the adjacent areas, namely MgO and BSTO1. Obviously, there is epitaxial growth of BSTO1 on MgO (001) where the (001) lattice planes of cubic BSTO are parallel to the (002) planes of MgO. Figure 8b exhibits a transition between BSTO1 and BSTO2 regions within the PLD-grown BSTO film. Again, the growth direction of the BSTO1 region is along the [001] zone axis as can be deduced from the diffractogram. In contrast, no clear information about any orientation relationship of the BSTO2 region is available, since its diffractogram shows a nanocrystalline

structure which is consistent with the NBD results presented above. The immediate transition between MgO and a BSTO2 region is imaged in Figure 8c, and it shows that the interface between BSTO2 and substrate marked with a dashed white line is very irregular due to the presence of a MgO island. Thus, owing to the three-dimensional island/layer configuration, there are contributions of both MgO and BSTO in the diffractogram obtained from this transition region including the MgO island.

To elucidate the element distribution and the chemical composition of the interface region between BSTO1 and BSTO2, EDXS analyses were performed in ROI 2 marked in Figure 6a. In particular, X-ray maps were recorded by combined STEM−EDXS with an electron probe smaller than 1 nm. The obtained map data were subsequently quantified. Moreover, after quantification of the maps line-profile analyses were carried out for selected regions of the BSTO/MgO specimen. **Figure 9**b−f represents typical results of the distribution of the elements Ba, Sr, Ti, Mg, and O in ROI 2. The element maps clearly allow differentiating between the MgO substrate and the BSTO film, where the interface between substrate and film is flat and chemically sharp in regions of the dominant BSTO1. However, at the nucleation site of the BSTO2 region an MgO island with a height of about 80 nm is observed. The presence of an MgO island is typical for all BSTO2 regions. This lets us conclude that the BSTO film up to a thickness of 80 nm contains only BSTO1, while both BSTO1
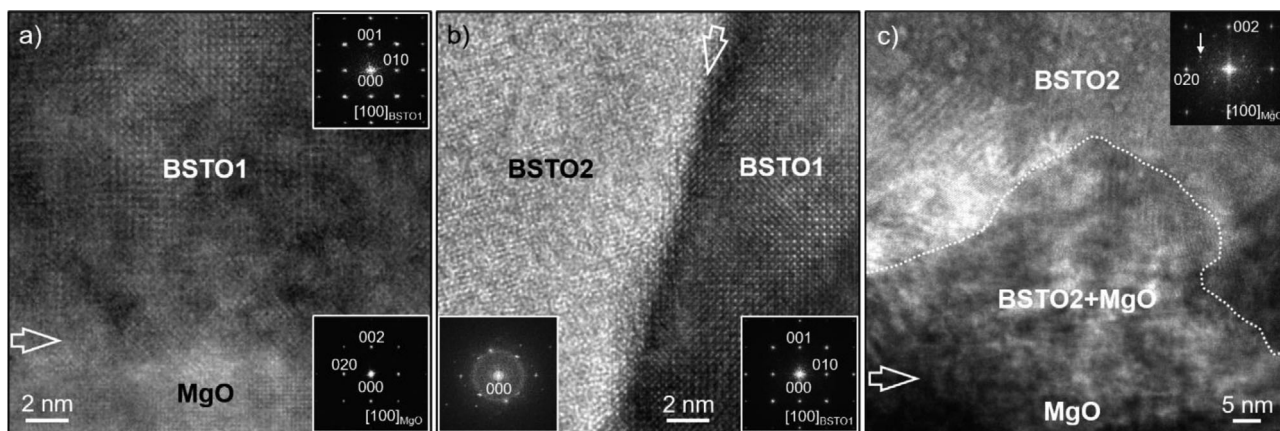
**ADVANCED
SCIENCE NEWS**

www.advancedsciencenews.com

CRYSTAL
Research&Technology

www.crt-journal.org

Figure 8. Structure analysis of the BSTO layer on MgO by high-resolution transmission electron microscopy (HRTEM) imaging. a) Structural peculiarities of a transition region between the MgO substrate and a BSTO1 region and b) of a BSTO1−BSTO2 interfacial region, the corresponding interfaces are marked with white arrows and the insets show diffractograms of the individual areas. c) HRTEM image shows a transition between MgO substrate and a BSTO2 region; the interface appears to be irregularly shaped and its assumable course is marked with a dashed white line.

and BSTO2 are detected above the dash-dotted line in Figure 9a. This transition detected for a film thickness larger than 80 nm using STEM−EXDS analysis is in accordance with the one determined by in situ 2D-RSMs recorded during the growth (cf. Section 3.1).

It has been reported in the literature[16] that getting MgO substrate for several hours up to 5 h at 850 °C would favor diffusion phenomena, which may cause the formation of islands. This annealing step of few hours before starting the growth of BSTO films was used for most of the cases to prepare such a fairly complicated in situ experiment and to align the experimental set-up.

From the quantified element map, a composition line profile is displayed in Figure 9g across the BSTO1−BSTO2 interfacial region (see the arrow in Figure 9a). In the profile, the differences in the element composition between the two BSTO regions are clearly revealed. Accordingly, the region of BSTO2 can be recognized by its lower Ti and higher O contents, respectively, in comparison to the regions of BSTO1 on the left- and right-hand sides. Moreover, the chemical composition of the grain boundaries between BSTO1 and BSTO2 regions is quite different from that of BSTO1 and BSTO2. Compared to the BSTO2 region, at the boundary the O content is further increased and that of Ti is even further lowered. In addition, Ba is here slightly enriched, while Sr is slightly depleted. All these findings hint at some diffusion processes that occurred during layer deposition. In principle, not only the above-described BSTO1 and BSTO2 regions are present in the grown film, but also very small portions of a third BSTO3 region that is located at the grain boundaries between crystallites of BSTO1 and BSTO2.

In order to get a deeper insight into the microchemistry of the PLD-grown BSTO film, the element composition was determined at different positions. For EDXS quantification the thin-film approximation introduced by Cliff and Lorimer was applied,[12], i.e., only atomic-number correction of X-ray intensities was performed, but no correction of absorption and fluorescence phenomena. Consequently, especially the oxygen content can be underestimated due to stronger absorption of the low-energy O-K_α line (523 eV), which is more pronounced in thicker regions of the TEM lamella. In addition, the overlap of the Ti-

K and Ba-L lines can contribute to the error. For these reasons, the quantified data can only serve as coarse estimates showing relative differences in the local composition. The accuracy of the concentration values is not better than ±5 at% and, moreover, there are additional uncertainties owing to the above-mentioned absorption of the O-K_α radiation.

Exemplarily, the chemical composition of the BSTO film was determined in three selected areas 1−3, which are marked in Figure 9d. In comparison to the stoichiometry of the BSTO target, where the Ba and Sr atoms should have similar contents and the ratio Ti:O should be 1:3, the following composition values were found in regions 1−3:

1) In region 1 that corresponds to the MgO island, the measured element concentrations are approximately 45 at% Mg and 51 at% O, in addition to 1 at% Ba, 1 at% Sr, and 2 at% Ti.
2) Region 2 corresponds to a triangular-shaped region of BSTO2. The contents of Ba and Sr are nearly the same and close to 10 at%. However, compared to regions of BSTO1 (cf. area 3) the Ti content of approximately 22 at% is slightly lower and that of O (57 at%) is higher. The 1 at% missing to a total of 100 at% is related to Mg. An extremely small Mg-Kα X-ray peak can be observed in all spectra, which is probably an artifact caused by some MgO redeposition during the FIB preparation of the TEM lamella.
3) Region 3 (cf. Figure 9d) is located in an area of the dominant BSTO1. Here, the Ti concentration amounts to about 27 at% and that of O is about 51 at%. The Sr content (≈11 at%) appears to be marginally higher than that of Ba (≈10 at%) reflecting the formation of a slightly Sr-enriched BSTO region with Ba/Sr ≈ 0.91.

Moreover, the EDXS line profile (cf. Figure 9g) shows that there is a third region, namely the grain boundaries between BSTO1 and BSTO2, with a chemical composition that is relatively close to the stoichiometry of the target used for the PLD growth. In particular, the Ti and O contents amount to approximately 20 and 60 at%, respectively, and correspond to the expected Ti/O ratio of 1:3.
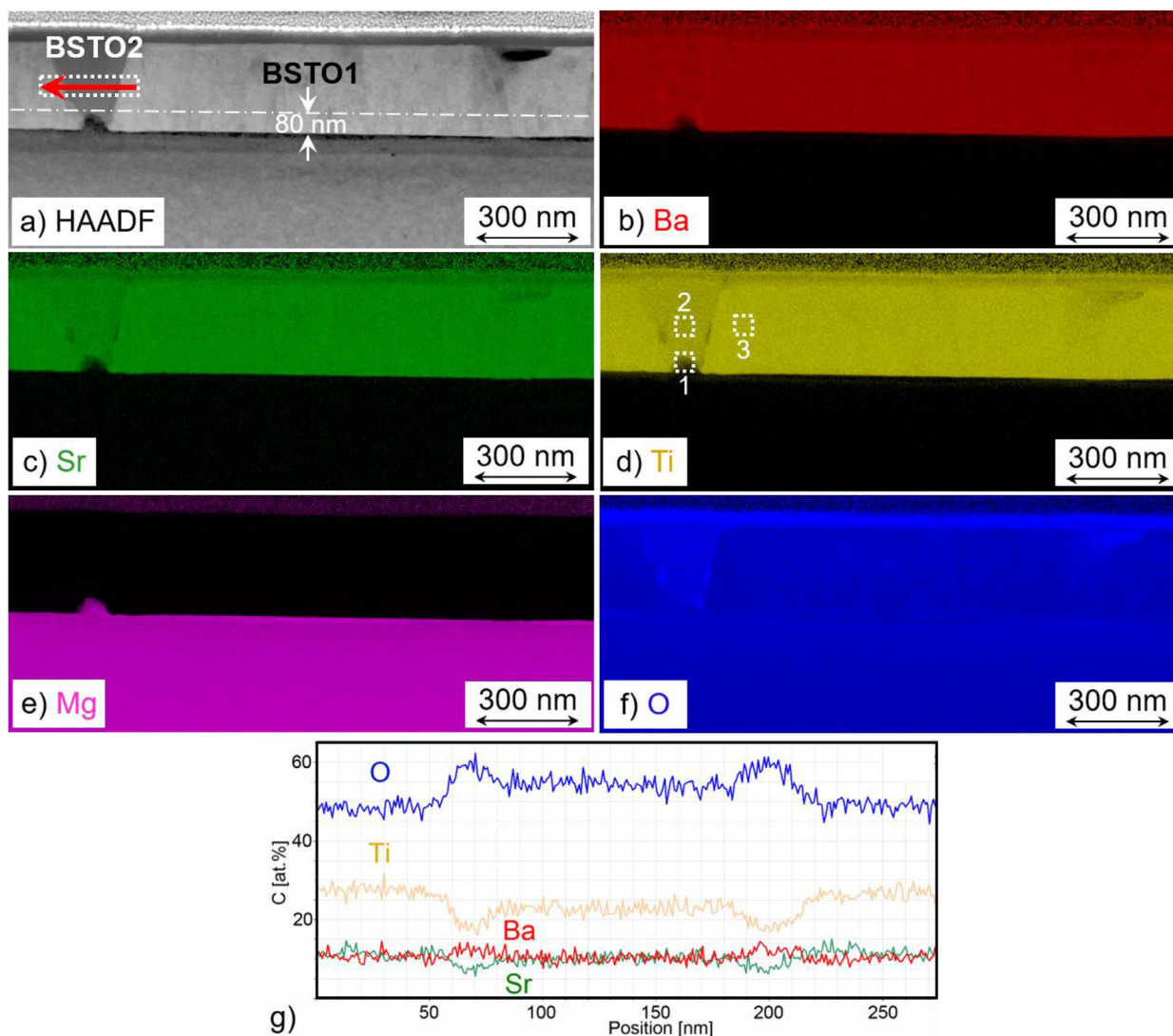
**ADVANCED
SCIENCE NEWS**

www.advancedsciencenews.com

CRYSTAL
Research&Technology

www.crt-journal.org

Figure 9. X-ray mapping and energy-dispersive X-ray spectroscopy (EDXS) line-profile analysis of the deposited BSTO film. a) Scanning transmission electron microscopy (STEM) high-angle annular dark-field (HAADF) image of the BSTO layer on MgO and corresponding distribution of the elements b) Ba, c) Sr, d) Ti, e) Mg, f) O, and g) quantified energy-dispersive X-ray spectroscopy (EDXS) line profile across the interfacial regions between BSTO1 and BSTO2 in ROI 1.

The formation of BSTO with different composition from a stoichiometric BSTO target during magnetron sputtering was already reported by Im et al.[17] They found a strong composition dependency of the resulting about 80 nm thick BSTO films on the (Ar + O$_2$) gas pressure. Particularly, the ratio of (Ba + Sr)/Ti changed from 0.73 to 0.98 for a variation in the total gas pressure from 22 to 58 mTorr. In the case of our BSTO layer, the oxygen pressure in the chamber was set to 200 mTorr, and it is very likely that the specific microstructure of the MgO substrate with its nanosized islands on top locally influenced the BSTO growth during PLD growth. Moreover, one can conclude that the difference in the lattice parameters recorded by in situ XRD analysis for the two BSTO1 and BSTO2 regions is mainly due to the variation in the corresponding composition as it is determined by STEM−EDXS.

4. Conclusions

In situ XRD study combined with in situ RHEED was used complementarily to characterize the growth mechanism of BSTO on MgO at P_{O2} = 200 mTorr and at T = 850 °C and to follow the evolution of the crystalline structure with the film thickness. By monitoring the diffraction profile of XRD002, it was possible to determine the in-plane residual strain and the crystalline structure parameters. This had allowed us to detect a transition between BSTO1 and BSTO2. Despite that the in situ RHEED could be coupled to the in situ XRD RSMs for a film thickness below Th = 80 nm, it was possible to determine that the mixed growth is the growth mode of BSTO. This was also confirmed by the variation of the out-of-plane and in-plane lattice parameters as a function of the thickness. By means of 3D time-resolved

diffraction intensity variation, two growth periods were revealed where the diffraction intensity of XRD002 (proportional to the growth intensity) varies linearly in period I and exponentially in period II. This could be related to a transition in the crystalline structure as the film thickness is larger than 80 nm. As a consequence, in situ XRD was proved to be a reliable and powerful diagnostic tool to measure the crystal transformation in terms of transition from one single crystalline region to two crystalline BSTO regions. This transition occurred for a film thickness in the range from 80 to 100 nm. Our investigations show that the grown BSTO film consists of two crystalline regions characterized by different lattice parameters, tetragonal distortion, and in-plane residual strain when the film thickness exceeds $Th = 100$ nm. The existence of BSTO1 and BSTO2 led to two crystalline regions with partly different crystal structure, grain orientation, and chemical composition as it could be confirmed by ex situ TEM investigations. In more detail, by using NBD and the corresponding pattern simulation, it was possible for us to demonstrate the presence of a dominant BSTO1 region, having a very close stoichiometry and crystal structure to the used BSTO target, and a less dominant BSTO2 region which is more or less nanocrystalline and has a lower Ti content and higher O content compared to BSTO1. Evidently, as proved by HRTEM and STEM-EDXS the occurrence of BSTO2 regions is directly connected with the positions of small MgO islands that had formed on the substrate during annealing of the sample before PLD growth. In accordance, this difference in the structure/stoichiometry of BSTO1-rich and BSTO2-rich areas, respectively, induces differences in the resulting lattice parameters as it was recorded by in situ 2D-RSMs during the growth.

Acknowledgements

Conflict of Interest

The authors declare no conflict of interest.

[1] W. Chang, L. M. B. Alldredge, S. W. Kirchoefer, J. M. Pond, *J. Appl. Phys.* **2007**, *102*, 014105.

[2] L. M. B. Alldredge, W. Chang, S. B. Qadri, S. W. Kirchoefer, J. M. Pond, *Appl. Phys. Lett.* **2007**, *90*, 212901.

[3] X. H. Zhu, Q. D. Meng, L. P. Yong, Y. S. He, B. L. Cheng, D. N. Zheng, *J. Phys. D: Appl. Phys.* **2006**, *39*, 2282.

[4] W. J. Kim, H. D. Wu, W. Chang, S. B. Qadri, J. M. Pond, S. W. Kirchoefer, D. B. Chrisey, J. S. Horwitz, *J. Appl. Phys.* **2000**, *88*, 5448.

[5] Z. G. Ban, S. P. Alpay, *J. Appl. Phys.* **2002**, *91*, 9288.

[6] J. Belloti, E. K. Akdogan, A. Safari, W. Chang, S. Kichoefer, *Integr. Ferroelectr.* **2002**, *49*, 113.

[7] J. H. Gruenewald, J. Nichols, S. S. A. Seo, *Rev. Sci. Instrum.* **2013**, *84*, 043902.

[8] A. Fluri, D. Pergolesi, V. Roddatis, A. Wokaun, T. Lippert, *Nat. Commun.* **2016**, *7*, 10692.

[9] P. J. Mousley, C. W. Burrows, M. J. Ashwin, M. Takahasi, T. Sasaki, G. R. Bell, *Phys. Status Solidi B* **2017**, *254*, 1600503.

[10] S. Bauer, A. Rodrigues, T. Baumbach, *Sci. Rep.* **2018**, *8*, 11969.

[11] G. Cliff, G. W. Lorimer, *J. Microsc.* **1975**, *103*, 203.

[12] A. Segmüller, *J. Vac. Sci. Technol., A* **1991**, *9*, 2477.

[13] S. Bauer, A. Rodriguez, V. Holý, X. Jin, R. Schneider, T. Baumbach, unpublished.

[14] W. Chang, Ch. M. Gilmore, W. J. Kim, J. M. Pond, S. W. Kirchoefer, S. B. Qadri, D. B. Chirsey, J. S. Horwitz, *J. Appl. Phys.* **2000**, *87*, 3044.

[15] V. M. Mukhortov, Yu. I. Golovko, S. V. Biryukov, A. Anokhin, Y. I. Yuzyuk, *Tech. Phys.* **2016**, *61*, 91.

[16] A. F. Dégardin, F. Houzé, A. J. Kreisler, *IEEE Trans. Appl. Supercond.* **2003**, *13*, 2721.

[17] J. Im, O. Auciello, P. K. Baumann, S. K. Streiffer, D. Y. Kaufman, A. R. Krauss, *Appl. Phys. Lett.* **2000**, *76*, 625.